CMS Physics Analysis Summary

Contact: cms-pag-conveners-higgs@cern.ch 2016/07/25

Searches for invisible Higgs boson decays with the CMS detector

The CMS Collaboration

Abstract

Searches for invisible decays of the Higgs boson are presented. The data collected with the CMS detector at the LHC correspond to integrated luminosities of 5.1, 19.7, and 2.3 fb^{-1} at centre-of-mass energies of 7, 8, and 13 TeV, respectively. The search channels target Higgs boson production via gluon fusion, vector boson fusion, and in association with a vector boson. Upper limits are placed on the branching fraction of the Higgs boson decay to invisible particles, as a function of the assumed production cross sections. The combination of all channels, assuming standard model production cross sections, yields an observed (expected) upper limit on the invisible branching fraction of 0.24 (0.23) at a 95% confidence level. The results are also interpreted under Higgs-portal dark matter models.

1 Introduction

The discovery of the Higgs boson (H) and the study of its properties by the ATLAS and CMS Collaborations [1–3] at the CERN LHC have placed major constraints on potential models of new physics beyond the standard model (SM). Precision measurements of the couplings of the Higgs boson from a combination of the 7 and 8 TeV ATLAS and CMS data sets indicate a very good agreement between the measured properties of the Higgs boson and the SM predictions [4]. In particular, these measurements provide indirect constraints on additional contributions to the Higgs boson width from non-SM decay processes. The resulting indirect upper limit on the Higgs branching fraction to non-SM decays is 0.34 at a 95% confidence level (CL) [4].

A number of models for physics beyond the SM allow for invisible decay modes of the Higgs boson, such as decays to neutralinos in supersymmetric models [5] or graviscalars in models with extra spatial dimensions [6, 7]. More generally, invisible Higgs decay modes can be realised through the interactions between the Higgs boson and the dark matter (DM) sector. In the "Higgs-portal" models [8–11], the Higgs boson acts as a mediator between the SM and DM particles allow for direct production of DM at the LHC. Furthermore, cosmological models that propose that the Higgs boson played a central role in the evolution of the early universe, motivate the study of the relationship between the Higgs boson and DM [12, 13].

Direct searches for invisible decays of the Higgs boson provide increased sensitivity to the invisible Higgs boson width beyond the indirect constraints. These searches are possible at the LHC when the Higgs boson recoils against a visible system. Previous searches by the ATLAS and CMS Collaborations have targeted Higgs production in association with a V (= W or Z) boson (VH) [14–16] or with jets consistent with a vector boson fusion (qqH) topology [16, 17]. Additionally, searches for DM in events with missing energy plus jets have been interpreted as a Higgs boson produced via gluon fusion and decaying to invisible particles [18].

In this document, results from a combination of searches for invisible decays of the Higgs boson, using data from Run 1 (2011 and 2012) and Run 2 (2015) of the LHC are presented. The searches target the qqH production mode and the VH production mode. The searches in the VH production mode include searches targeting ZH production, in which the Z boson decays to a pair of leptons (either e^+e^- or $\mu^+\mu^-$), or $b\bar{b}$, and searches in the ZH and WH production modes, in which the W or Z boson decays hadronically. A similar combination of direct searches in these channels, by the ATLAS Collaboration, yields an upper limit of 0.25 on the Higgs boson invisible branching fraction, $B(H \to \text{inv.})$ [19]. Additional sensitivity is achieved by including a search targeting gluon fusion production (ggH) in association with initial-state radiation (ISR), as shown in. The diagrams for the qqH, VH and ggH Higgs production processes are shown in Fig. 1.

This document is structured as follows: an overview of the event reconstruction is given in Section 2 and the datasets and simulation used for the searches are presented in Section 3. In Section 4, the strategy for each search included in the combination is described, and in Section 5 the results of the searches are presented and interpreted in terms of upper limits on $B(H \to \text{inv.})$. Finally, the conclusions are presented in Section 6.

2 Event reconstruction

Objects are reconstructed using the CMS particle-flow (PF) algorithm [20, 21], which optimally combines information from the various detector components to reconstruct and identify indi-

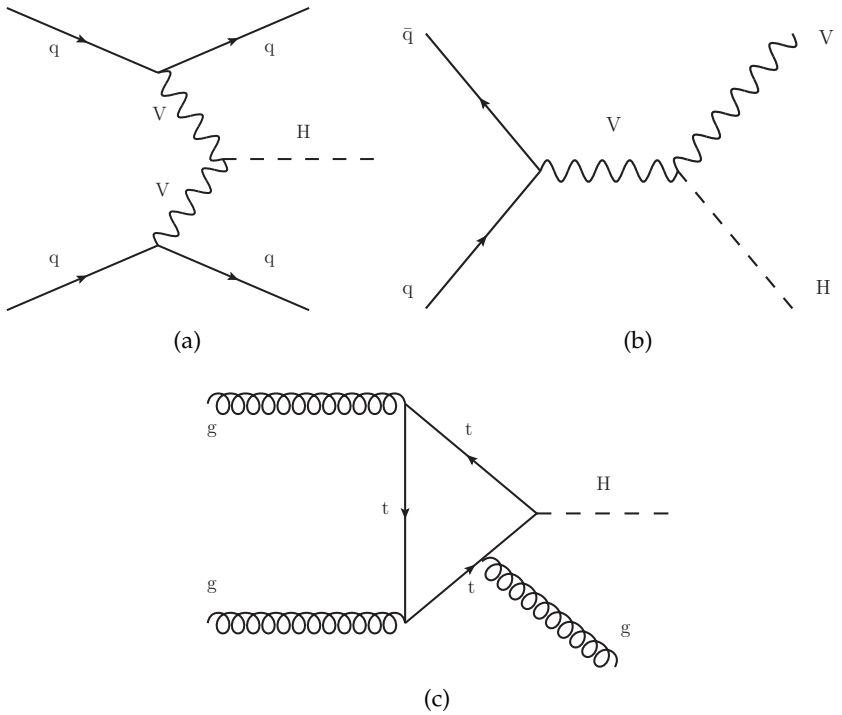

Figure 1: Diagrams for Higgs boson production in the (a) qqH, (b) VH, and (c) ggH in association with ISR modes.

vidual particles. The interaction vertex with the maximum value of $\sum_i p_{\mathrm{T}i}^2$, where $p_{\mathrm{T}i}$ is the transverse momentum of the i-th track associated with the vertex, is selected as the reference vertex for the reconstruction of these objects.

Jets are reconstructed by clustering PF candidates, using the anti-k_t algorithm [22] with a distance parameter of 0.5 (0.4) for the 7 and 8 (13) TeV dataset. Analyses exploring Lorentz-boosted hadronic objects employ large-radius jets, clustered using the Cambridge–Aachen algorithm at 13 TeV and the anti-k_t algorithm at 8 TeV, using a distance parameter of 0.8. The combined secondary vertex (CSV) algorithm is used to identify jets originating from b quarks [23–25].

The jet momentum is corrected to account for contamination from additional interactions in the same bunch crossing (pileup, PU) based on the event energy density scaled proportionally to the jet area [26].

Calibrations based on simulation and control samples in data are applied to correct the absolute scale of the jet energy [27]. The jets are further subjected to a standard set of identification criteria [28]. All jets are required to have $p_{\mathrm{T}} > 30$ GeV and $\eta < 4.7$, unless stated otherwise.

The missing transverse momentum vector $\vec{p}_{\mathrm{T}}^{\,\mathrm{miss}}$ is defined as the projection on the plane perpendicular to the beams of the negative vector sum of the momenta of all PF candidates in the event. The magnitude of $\vec{p}_{\mathrm{T}}^{\,\mathrm{miss}}$ is referred to as $E_{\mathrm{T}}^{\mathrm{miss}}$.

Electron (e), photon (γ), and muon (μ) candidates are required to be within the relevant detector acceptances of $|\eta| < 2.5$ (e/γ) and $|\eta| < 2.4$ (μ). Electron and photon candidates in the transition region between the ECAL barrel and endcap ($1.4442 < |\eta| < 1.566$) are not considered. Details of the electron, photon, and muon reconstruction algorithms and their performance can be found in Refs. [29], [30], and [31], respectively.

Lepton isolation is based on the sum of the momenta of additional PF candidates in a cone of

radius $R = \sqrt{(\Delta\eta)^2 + (\Delta\phi)^2} = 0.4$ around each lepton, where $\Delta\phi$ and $\Delta\eta$ are the differences in azimuthal angle and pseudorapidity between the lepton and each particle in the sum, respectively. The isolation sum is required to be smaller than 15% (12%) of the electron (muon) p_{T}. In order to reduce the dependence of the isolation variable on the number of PU interactions, charged hadrons are only included in the sum if they are consistent with originating from the selected primary vertex of the event. To correct for the contribution from PU events to the isolation sum in the case of electrons, the median energy density, determined on an event-by-event basis as described in Ref. [32], is subtracted from the sum. For muons the correction is made by subtracting half the sum of the p_{T} of charged particles inside the cone that are not associated with the primary vertex.

Details of the reconstruction of τ leptons can be found in Ref. [33]. The sum of the momenta of all particles within a cone of radius $\Delta R < 0.3$ around the τ candidates is required to be less than 5 GeV.

3 Data samples and simulation

The data used for the analyses comprise pp collisions collected with the CMS detector in both the 2011 and 2012 Run 1, and 2015 Run 2 data taking periods of the LHC. The integrated luminosities are 4.9 fb^{-1}, 19.7 fb^{-1} and 2.3 fb^{-1} at centre of mass energies of $\sqrt{s} = 7,\ 8$, and 13 TeV respectively. The uncertainties in the integrated luminosity measurements are 2.2%, 2.6%, and 2.2% at 7 [34], 8 [35], and 13 TeV [36], respectively.

All signals are generated assuming a Higgs boson mass of 125 GeV, consistent with the combined ATLAS and CMS measurement of the Higgs boson mass [37]. The SM Higgs cross sections at 125 GeV and their uncertainties for all production mechanisms are taken from Ref. [38] at all centre-of-mass energies. Simulated ggH and qqH events are generated with POWHEG1.0 (POWHEG2.0) [39–41] interfaced with PYTHIA6.4 [42] (PYTHIA8.1 [43]) at 7 and 8 (13) TeV. The inclusive cross sections for the ggH and qqH production modes are calculated at next-to-next-to-next-to-leading-order (N3LO) QCD + NLO electroweak [44] and NNLO QCD + NLO electroweak precisions [45], respectively. In the 8 TeV sample, the p_{T} distribution of the Higgs boson in the ggH process is reweighted to match the next-to-next-to-leading-order (NNLO) plus next-to-next-to-leading-logarithmic (NNLL) prediction from HRES2.1 [46, 47]. The event generation at 13 TeV is tuned so that the p_{T} distribution agrees between POWHEG2.0 and HRES2.1. Associated VH production is generated using PYTHIA6.4 (PYTHIA8.1) at 7 and 8 (13) TeV and normalised to an inclusive cross section calculated at NNLO QCD and NLO electroweak precision [45]. The expected contribution from $\mathrm{gg} \to \mathrm{ZH}$ production is estimated using events generated with POWHEG2.0 interfaced with PYTHIA8.1.

The majority of background samples, including W+jets, Z+jets, $\mathrm{t\bar{t}}$, and triboson production, are generated using MADGRAPH5.1 [48] (MADGRAPH5_AMC@NLO2.2 [49]) with LO precision, interfaced with PYTHIA6.4 (PYTHIA8.1) for description of hadronisation and fragmentation in the 7 and 8 (13) TeV analyses. Single top quark event samples are produced using POWHEG1.0 [50] and diboson samples are generated using PYTHIA6.4 (PYTHIA8.1) at 7 and 8 (13) TeV. Multijet QCD events are generated using either PYTHIA6.4 or MADGRAPH5_AMC@NLO2.2, depending on the analysis. All signal and background samples use the CTEQ6L [51] (NNPDF3.0 [52]) parton distribution functions (PDFs) at 7 and 8 (13) TeV. The underlying event simulation is done using parameters from the Z2* tune [53, 54] and the CUETP8M1 tune [54] for PYTHIA6.4 and PYTHIA8.1, respectively.

The interactions of all final-state particles with the CMS detector are simulated with GEANT4 [55].

The simulated samples include PU interactions with the multiplicity of reconstructed primary vertexes matching that in the relevant datasets. An uncertainty of 5% in the total inelastic pp cross section is propagated to the PU distribution and is treated as correlated between the data taking periods.

4 Channels included in the combination

The characteristic signature of invisible Higgs boson decays for all of the included searches is a large $E_{\mathrm{T}}^{\mathrm{miss}}$, with the $\vec{p}_{\mathrm{T}}^{\mathrm{miss}}$ recoiling against jets or leptons, consistent with one of the production topologies. In order to reduce the contributions expected from the SM backgrounds, the properties of the visible recoiling system are exploited. The events are divided into several exclusive categories designed to target a particular production mode. In addition to the channels described in the following sections, an 8 TeV analysis targeting ZH production in which the Z boson decays to a $\mathrm{b\bar{b}}$ pair [16] is included in this combination. A summary of the analyses included in the combination and the expected signal composition in each of them are given in Table 1. The signal in the vector-boson fusion (VBF) analysis is dominated by qqH production and the expected signals in the $\mathrm{Z}(l^+l^-)$ and $\mathrm{Z}(\mathrm{b\bar{b}})$ analyses are composed entirely of ZH production. In contrast, the V(jj)-tagged and monojet searches, which target events with a central, Lorentz-boosed jet, contain a mixture of the different production modes. This is due to the limited information in the jets used to categorise these events. As shown in Table 1, the signal composition is similar across the 7, 8, and 13 TeV datasets, except for the V(jj)-tagged analysis where the ZH contribution is larger, relative to the WH contribution, in the 13 TeV analysis. This is because the lepton veto requirement at 13 TeV is less efficient at removing leptonic Z decays in the case where the lepton pair is produced at high Lorentz boost causing the two leptons to overlap.

Table 1: Summary of the expected composition of production modes of a Higgs boson with the mass of 125 GeV in each analysis included in the combination. The relative contributions assume SM production cross sections.

Analysis Tag		$\int \mathcal{L}$ (fb^{-1})			Expected Signal Composition (%)	
		7 TeV	8 TeV	13 TeV	7 or 8 TeV	13 TeV
qqH-tagged	VBF	–	19.2 [16]	2.3	7.8 (ggH), 92.2 (qqH)	9.1 (ggH), 90.9 (qqH)
VH-tagged	$\mathrm{Z}(l^+l^-)$	4.9 [16]	19.7 [16]	2.3	100 (ZH)	
	$\mathrm{Z}(\mathrm{b\bar{b}})$	–	18.9 [16]	–	100 (ZH)	
	V(jj)-tagged	–	19.7 [56]	2.3	25.1 (ggH), 5.1 (qqH), 23.0 (ZH), 46.8 (WH)	38.7 (ggH), 7.1 (qqH), 21.3 (ZH), 32.9 (WH)
ggH-tagged	monojet	–	19.7 [56]	2.3	70.4 (ggH), 20.4 (qqH), 3.5 (ZH), 5.7 (WH)	69.4 (ggH), 21.9 (qqH), 4.2 (ZH), 4.6 (WH)

4.1 The VBF analysis

The VBF Higgs boson production is characterised by the presence of two jets with a large separation in pseudorapidity and a large invariant mass ($\mathrm{m_{jj}}$). The selection of events targeting VBF production exploits this distinctive topology to give good discrimination between the invisible decays of a Higgs boson and the large SM backgrounds. The contributions from the dominant $\mathrm{Z}(\nu\nu)$+jets and $\mathrm{W}(l\nu)$+jets backgrounds and the QCD multijet backgrounds are estimated using data control regions. A simultaneous fit is performed to the observed event yields in each region, to extract any potential signal and place upper limits on $\mathrm{B}(\mathrm{H} \to \mathrm{inv.})$. The 8 TeV analysis improves on the previous analysis [16] by using additional data samples from high rate

triggers installed in CMS in 2012. These triggers wrote to a special data stream and the events were reconstructed during the long shutdown of the LHC in 2013 [57]. The event selection was also simplified, making it more similar to the 13 TeV analysis described in detail below.

4.1.1 Event selection

Events are selected online using a dedicated VBF trigger, in both the 8 and 13 TeV datasets, with thresholds optimised for the instantaneous luminosities during each data taking period. The trigger requires a forward/backward pair of jets with a pseudorapidity separation of $|\Delta\eta(j_1, j_2)| > 3.5$ and a large invariant mass. For the majority of the 8 TeV data taking period the thresholds used were $p_T > 30$ or 35 GeV, depending on the LHC conditions, and $m_{jj} > 700$ GeV. For the 13 TeV data set, these were modified to $p_T^{j_1,j_2} > 40$ GeV and $m_{jj} > 600$ GeV. In addition, the trigger requires the presence of missing transverse energy, reconstructed using the ECAL and HCAL information only. The thresholds were $E_T^{miss} > 40$ (140) GeV at 8 (13) TeV. The efficiency of the trigger was measured as a function of the main selection variables: $p_T^{j_1,j_2}$, m_{jj}, and E_T^{miss}. A parameterisation of this efficiency is then applied as a weight to simulated events. The subsequent selection after the full reconstruction is designed to maintain the trigger efficiency greater than 80%.

The selection of events for the signal region is optimised for VBF production of the Higgs boson with the mass of 125 GeV, decaying to invisible particles. Events are required to contain at least two jets inside the tracker acceptance $|\eta| < 4.7$ with oppositely-signed pseudo-rapidities, separated by $|\Delta\eta(j_1, j_2)| > 3.6$. The two jets in the event with the largest p_T satisfying this requirement form the dijet pair. The leading and subleading jets in this pair are required to have $p_T^{j_1,j_2} > 50(80)$, $45(70)$ GeV and dijet invariant mass $m_{jj} > 1200$ (1100) GeV at 8 (13) TeV. Events are required to have E_T^{miss} greater than 90 (200) GeV at 13 TeV (8 TeV). Identified muons are removed from the calculation of E_T^{miss}. For the 8 TeV dataset, an additional requirement on the significance of the missing transverse energy, $\sigma(E_T^{miss}) > 4$, further aids the separation between the signal and background. The variable $\sigma(E_T^{miss})$ is defined as the ratio of E_T^{miss} to the square root of the scalar sum of the transverse energy of all PF objects in the event.

In order to reduce the large backgrounds from QCD multijet production, the jets in the event are required to be recoiling against the missing transverse momentum. The azimuthal angle between $\vec{p}_T^{miss}$ and each jet in the event, $\Delta\phi(\vec{p}_T^{miss}, j)$, is determined. The minimum value of $\Delta\phi(\vec{p}_T^{miss}, j)$ is required to be greater than 2.3. Finally, events containing at least one loosely identified muon or electron with $p_T > 10$ GeV are rejected to suppress backgrounds from leptonic vector boson decays.

A summary of the event selection used in the 8 and 13 TeV datasets is given in Table 2. Figure 2 shows the distribution of $\Delta\eta(j_1, j_2)$ and m_{jj} in data and the predicted background contributions after the selection. The contribution expected from a Higgs boson with a mass of 125 GeV, produced assuming SM cross sections and decaying to invisible particles with 100% branching fraction is also shown. The backgrounds have been normalised using the results of the simultaneous fit, as described in Section 4.1.2.

4.1.2 Background estimation

The dominant backgrounds to this search arise from $Z(\nu\nu)$+jets events and $W(l\nu)$+jets events with the charged lepton outside of the detector acceptance or not identified. These backgrounds are estimated using data control regions, in which a Z or W boson, produced in association with the same dijet topology, decays to well-identified charged leptons. These control regions are designed to be as similar to the signal region as possible to limit the extrapolation required be-

Table 2: Event selections for the VBF invisible Higgs boson decay search at 8 and 13 TeV.

	8 TeV	13 TeV
$p_T^{j_1}$	> 50 GeV	> 80 GeV
$p_T^{j_2}$	> 45 GeV	> 70 GeV
m_{jj}	> 1200 GeV	> 1100 GeV
E_T^{miss}	> 90 GeV	> 200 GeV
$\sigma(E_T^{miss})$	> 4	–
$\min\Delta\phi(\vec{p}_T^{miss}, j)$	> 2.3	
$\Delta\eta(j_1, j_2)$	> 3.6	

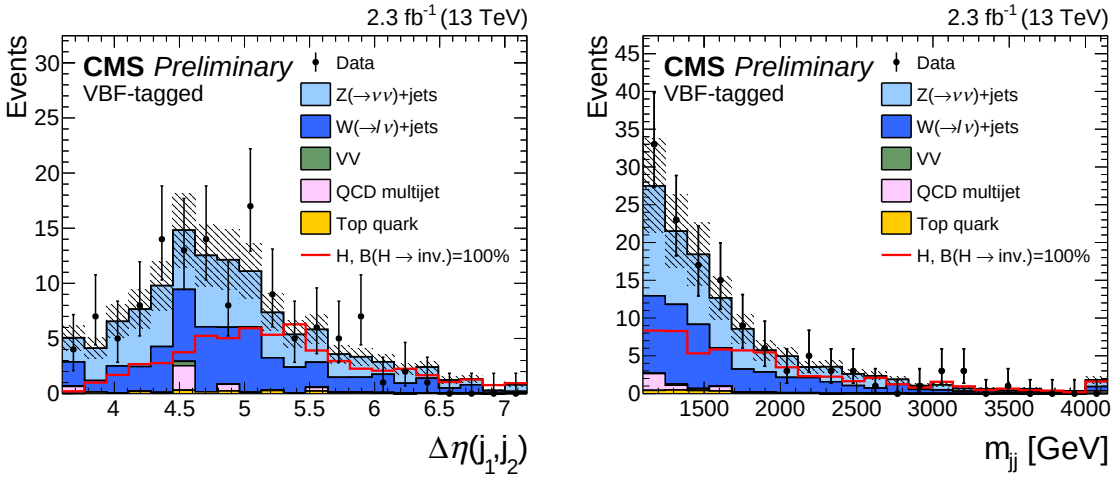

(a) (b)

Figure 2: Distributions of (a) $\Delta\eta(j_1, j_2)$ and (b) m_{jj} in the VBF signal region for data and simulation. The background yields are scaled to their post-fit values, with the total post-fit uncertainty represented as the black hatched area. The last bin contains the overflow events. The expected contribution from a Higgs boson with a mass of 125 GeV, produced with the SM cross section and decaying to invisible particles with 100% branching fraction is shown in red.

tween different kinematic phase spaces. An additional control region, enriched in QCD multijet events, is defined to estimate the contribution arising due to mismeasured jet energies causing apparent E_T^{miss}. Additional, smaller contributions, due to diboson production and $t\bar{t}$ and single top quark production are estimated directly from simulation.

A dimuon control region is defined, enriched in $Z \to \mu^+\mu^-$ events, requiring a pair of opposite charged muons with $p_T > 20$ GeV, $|\eta| < 2.1$, and an invariant mass $m_{\mu\mu}$ in the range 60–120 GeV. Three single-lepton regions (one enriched in each of the $W \to e\nu$, $W \to \mu\nu$, and $W \to \tau\nu$ processes) are defined by removing the lepton veto and requiring precisely one isolated lepton, with $p_T > 20$ GeV, of a given flavour, and no additional leptons. The lepton is required to be within the pseudorapidity range of $|\eta| < 2.1$, 2.4, or 2.3 for the single-muon, single-electron, or single τ lepton region, respectively. The remaining jets and E_T^{miss} criteria are identical to the signal region, except in the $W \to \tau\nu$ control region where the $\min\Delta\phi(\vec{p}_T^{miss}, j)$ criterion is relaxed to $\min\Delta\phi(\vec{p}_T^{miss}, j) < 1$, taking the minimum over the leading two jets only, to ensure QCD multijet events are suppressed, while retaining sufficient number of events in the con-

trol region. Additionally, a requirement that $\min\Delta\phi(\vec{p}_{\mathrm{T}}^{\,\mathrm{miss}},\mathrm{j}) < 2.3$ is applied to maintain an orthogonal selection to the signal region.

Finally, additional control regions are defined in data that are identical to the signal region selection except for the requirement on $\min\Delta\phi(\vec{p}_{\mathrm{T}}^{\,\mathrm{miss}},\mathrm{j})$. In the 13 TeV analysis, an independent control region is defined by a requirement of $\min\Delta\phi(\vec{p}_{\mathrm{T}}^{\,\mathrm{miss}},\mathrm{j}) < 0.5$ to enrich the QCD multijet contribution. In the 8 TeV analysis, a two-step procedure is used in which two control regions are defined. The first control region requires $\min\Delta\phi(\vec{p}_{\mathrm{T}}^{\,\mathrm{miss}},\mathrm{j}) < 1$ in which data, after subtracting contributions from other backgrounds, are used to determine the distribution of $\sigma(E_{\mathrm{T}}^{\mathrm{miss}})$ for QCD multijets. The distribution is normalised using events in a second region defined as $3 < \sigma(E_{\mathrm{T}}^{\mathrm{miss}}) < 4$ and $1 < \min\Delta\phi(\vec{p}_{\mathrm{T}}^{\,\mathrm{miss}},\mathrm{j}) < 2$, where the signal contribution is expected to be negligible. The integral of the normalised distribution in the region $\sigma(E_{\mathrm{T}}^{\mathrm{miss}}) > 4$ provides the estimate of the QCD multijet contribution in the signal region. Systematic uncertainties of 80% and 100% are assigned at 8 (13) TeV to account for potential biases in the extrapolation to the signal region.

Several sources of experimental systematic uncertainties are included in the predictions of the background components. The dominant ones are the jet energy scale and resolution [28] uncertainties, which are also propagated to the calculation of the $E_{\mathrm{T}}^{\mathrm{miss}}$, resulting in the background uncertainty of up to 8%, depending on the specific background. Smaller uncertainties are included to account for the PU description and lepton reconstruction efficiencies. Due to the looser selection applied in the $\mathrm{W} \to \tau\nu$ control region compared to the signal region, an additional systematic uncertainty of 20% in the prediction of the $\mathrm{W} \to \tau\nu$ contribution is included. Finally, additional cross section uncertainties of 7% (10%) [58–60] for diboson production and 10% (20%) [61–63] for the top quark background at 8 (13) TeV are included.

A maximum likelihood fit is performed simultaneously across each of the control regions, taking the expected background yields from simulation and observed event counts as inputs to the fit. Two scale factors are included as free parameters in the fit, one scaling both the W+jets and Z+jets processes and one scaling the QCD multijet yields across all of the regions. The fit is thereby able to constrain the contributions from W+jets, Z+jets, and QCD multijets directly from data.

The ratio of $\mathrm{W}(l\nu)$+jets to $\mathrm{Z}(\nu\nu)$+jets is calculated using simulated samples, generated with LO precision. Separate samples are produced for the production of the V-boson via quark-quark annihilation (QCD vertex) and production through V-boson fusion (electroweak vertex). A theoretical systematic uncertainty in the expected ratio of the $\mathrm{W}(l\nu)$+jets to $\mathrm{Z}(\nu\nu)$+jets yields was derived by comparing LO and NLO predictions after applying the full VBF kinematic selection using events generated with MADGRAPH_AMC@NLO2.2 interfaced with PYTHIA8.1, excluding events produced via VBF. A difference of 30% is observed between the ratios predicted by the LO and NLO calculations and is included as a systematic uncertainty in the ratio of the W+jets to Z+jets contributions. The ratio of the production cross sections of $\mathrm{W}(l\nu)$+jets to $\mathrm{Z}(\nu\nu)$+jets through electroweak vertices was compared at NLO and LO precision using VBF@NLO2.7 [64, 65] and found to agree within the 30% systematic uncertainty assigned.

The observed yields in data for each of the control regions, in the 13 TeV dataset, and the expected contributions from the backgrounds after the fit, ignoring the signal region events, are given in Table 3.

Table 3: Post-fit yields for the control regions and signal region of the VBF analysis using the 13 TeV dataset. The fit ignores the constraints due to the data in the signal region. For the W and Z processes, jet production through QCD or electroweak (EW) vertices are listed as separate entries. The signal yields shown assume SM ggH and qqH production rates for a Higgs boson with a mass of 125 GeV, decaying to invisible particles with $B(H \to \text{inv.}) = 100\%$

Process		Signal region	Control regions				
			single e	single μ	single τ	$\mu^+\mu^-$	QCD
$Z(\mu^+\mu^-)$+jets	QCD	–	–	–	–	4.2 ± 1.1	–
	EW	–	–	–	–	2.0 ± 0.7	–
$Z(\nu\nu)$+jets	QCD	47 ± 12	–	–	–	–	–
	EW	21 ± 7	–	–	–	–	–
$W(\mu\nu)$+jets	QCD	13 ± 2	–	53 ± 5	0.40 ± 0.19	–	45 ± 5
	EW	4.3 ± 0.8	–	27 ± 3	–	–	6.0 ± 0.9
$W(e\nu)$+jets	QCD	9.3 ± 1.5	17 ± 3	–	0.2 ± 2.2	–	39 ± 4
	EW	5.4 ± 1.1	7.8 ± 1.3	–	0.2 ± 0.13	–	6.1 ± 1.0
$W(\tau\nu)$+jets	QCD	13 ± 2	0.06 ± 0.06	–	12 ± 2	–	74 ± 9
	EW	5.5 ± 1.2	–	–	5.1 ± 1.2	–	24 ± 3
Top quark		2.3 ± 0.4	1.5 ± 0.3	6.8 ± 0.9	7.1 ± 1.0	0.22 ± 0.06	82 ± 11
QCD multijet		3 ± 23	–	5 ± 3	0.4 ± 0.3	–	1200 ± 170
Dibosons		0.7 ± 0.3	0.4 ± 0.4	0.8 ± 0.4	–	0.02 ± 0.02	1.8 ± 0.7
Total bkg.		125 ± 28	27 ± 3	91 ± 8	25 ± 4	6.4 ± 1.4	1500 ± 170
Data		126	29	89	24	7	1461
Signal	qqH	53.6 ± 4.9					
$m_H = 125$ GeV	ggH	5.4 ± 3.6					

4.2 $Z(ll)H$ analysis

The ZH production mode, where the Z boson decays to a pair of charged leptons, has a smaller cross section than qqH but a clean final state with lower background. The search targets events with a pair of same-flavour, opposite-charge leptons (l = e, μ), consistent with a leptonic Z boson decay, produced in association with a large E_T^{miss}. The background is dominated by the diboson processes, $ZZ \to llvv$ and $WZ \to lvll$ which contribute roughly 70% and 25% of the total background respectively.

In the 7 and 13 TeV datasets the sensitivity of the search is enhanced by using the distribution of the transverse mass of the dilepton-E_T^{miss} system, m_T defined as,

$$m_T = \sqrt{2\, p_T^{ll}\, E_T^{miss}\, \left(1 - \cos\Delta\phi(ll, \vec{p}_T^{miss})\right)}\,,$$

where p_T^{ll} is the transverse momentum of the dilepton system and $\Delta\phi(ll, \vec{p}_T^{miss})$ is the azimuthal angle between the dilepton system and the missing momentum vector. In the 8 TeV dataset, a two-dimensional fit is performed to the distributions of m_T and the azimuthal angle between the two leptons, $\Delta\phi(l,l)$ to exploit the increased statistical precision available in that dataset [16].

4.2.1 Event selection

Collision events are recorded using double electron and double muon triggers, with thresholds of $p_T^e > 17(12)$ GeV and $p_T^\mu > 17(8)$ GeV in 13 TeV and $p_T^{e,\mu} > 17(8)$ GeV in 8 TeV, for the leading (sub-leading) electron or muon, respectively. Single electron and single muon triggers are also

included in order to recover residual trigger inefficiencies.

Selected events are required to have two well-identified, isolated leptons with the same flavour and opposite charge (e^+e^- or $\mu^+\mu^-$) each with $p_T > 20$ GeV, and an invariant mass within the range 76−106 GeV. In the 13 TeV analysis, the $Z/\gamma^* \to l^+l^-$ background is substantially suppressed by requiring $\Delta\phi(l,l) < \pi/2$. As little hadronic activity is expected in the Z(ll)H final state, events with more than one jet with $p_T > 30$ GeV are rejected. Events containing a muon with $p_T > 3$ GeV and a b jet with $p_T > 30$ GeV are vetoed to reduce backgrounds from t-quark production. Diboson backgrounds are suppressed by rejecting events containing additional electrons or muons with $p_T > 10$ GeV. In the 13 TeV analysis, events containing a tau lepton with $p_T > 20$ GeV are vetoed to suppress the contributions from WZ $\to lvll$.

The remainder of the selection has been optimised for a Higgs boson with a mass of 125 GeV, produced in the Z(ll)H production mode. As a result of this optimisation, events are required to have $E_T^{miss} > 100$ (120) GeV, $\Delta\phi(ll, \vec{p}_T^{miss}) > 2.8$ (2.7) and $|E_T^{miss} - p_T^{ll}|/p_T^{ll} < 0.4(0.25)$, in the 13 TeV (8 and 7 TeV) datasets. Finally, the events are required to have $m_T > 200$ GeV. A summary of the event selection used for the 7, 8 and 13 TeV datasets is given in Tab. 4.

Table 4: Event selections for the Z(l^+l^-) Higgs invisible search using the 7, 8 TeV and 13 TeV datasets.

	13 TeV	7 and 8 TeV
$p_T^{e,\mu}$	> 20 GeV	
m_{ll}	76-106 GeV	
$\Delta\phi(l,l)$	$< \pi/2$	Fit $(-)$
E_T^{miss}	> 100 GeV	> 120 GeV
$\Delta\phi(ll, \vec{p}_T^{miss})$	> 2.8	> 2.7
$\Delta\phi(\vec{p}_T^{miss}, j)$	> 0.5[1]	$-$
$\lvert E_T^{miss} - p_T^{ll}\rvert/p_T^{ll}$	< 0.4	< 0.25
m_T	> 200 GeV	

[1] The $\Delta\phi(\vec{p}_T^{miss}, j)$ cut only applies in the 1-jet category.

The selected events are separated into two categories, events which contain no jets with $p_T > 30$ GeV and $|\eta| < 4.7$, and events which contain exactly one such jet. An additional selection requiring $\Delta\phi(\vec{p}_T^{miss}, j) > 0.5$ is applied in the 1-jet category at 13 TeV which significantly reduces the contribution from Z+jets.

The distribution of m_T for selected events in data and simulation, combining electron and muon events, for the 0-jet and 1-jet categories in 13 TeV are shown in Fig. 3.

4.2.2 Background estimation

The dominant backgrounds, ZZ $\to llvv$ and WZ $\to lvll$ are simulated at NLO using POWHEG2.0, for production via $q\bar{q}$, and MCFM7.0 [66] for the contribution from gg $\to$ ZZ with electroweak corrections applied. Uncertainties due to missing higher-order corrections for these processes are evaluated by varying the renormalisation and factorisation scales by a factor of two, yielding systematic uncertainties between 4 and 10%. A 2% uncertainty is added to account for the jet category migration due to PDF effects. Additional uncertainties are included in the gg $\to$ ZZ event yield to account for the uncertainties in the electroweak corrections.

The Z+jets background is estimated using a data control region dominated by single-photon

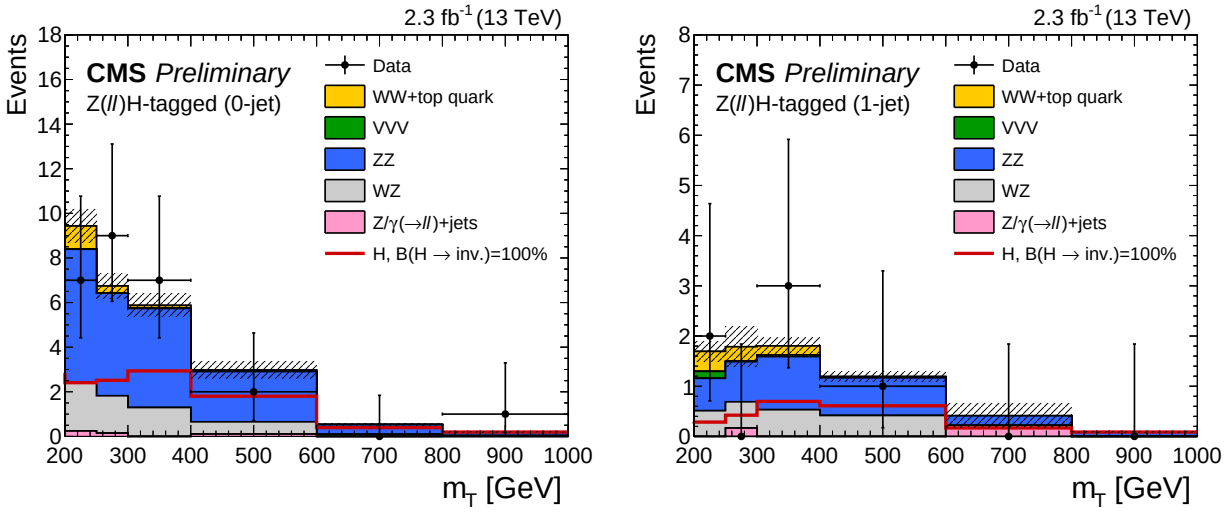

(a) (b)

Figure 3: Distributions of m_T in data and simulation for $Z(ll)H$ tagged events in the (a) 0-jet and (b) 1-jet categories at 13 TeV, combining dielectron and dimuon events. The background yields are normalised to 2.3fb^{-1}. The shaded bands represent the total statistical and systematic uncertainties in the backgrounds. The horizontal bars on the data points represent the width of the bin centred at that point. The expectation from a Higgs boson with a mass of 125 GeV, from ZH production, decaying to invisibles with a 100% branching fraction is shown in red.

production in association with jets (γ+jets). The γ+jets events have similar jet kinematics to $Z(l^+l^-)$+jets, but with a much larger production rate. The γ+jets events are weighted, as a function of the photon p_T, to match the distribution observed in $Z(l^+l^-)$+jets events in data. This accounts for the dependence of the E_T^{miss} on the hadronic activity. A systematic uncertainty of 100% is included in the final Z+jets background estimate to account for the limited statistics at large E_T^{miss} in the data used to weight the γ+jets events.

The remaining, nonresonant backgrounds are estimated using a control sample of events, selecting pairs of leptons of different flavour and opposite charge ($e^{\pm}\mu^{\mp}$) that pass all of the signal region selections. These backgrounds consist mainly of leptonic W boson decays in $t\bar{t}$ and tW processes, and WW events. Additionally, semileptonic τ decays contribute to these backgrounds. As the branching fraction to the $e^{\pm}\mu^{\mp}$ final states is twice that of the e^+e^- or $\mu^+\mu^-$ final states, the $e^{\pm}\mu^{\mp}$ control region provides precise estimates of the nonresonant backgrounds. In the 13 TeV analysis, the contribution from the nonresonant backgrounds is given by

$$N_{ll}^{bkg} = N_{e\mu}^{data}(k_{ee/\mu\mu} + 1/k_{ee/\mu\mu})/2\,,$$

where $N_{e\mu}^{data}$ is the number of events in the $e^{\pm}\mu^{\mp}$ control region after subtracting other backgrounds and $k_{ee/\mu\mu} = \sqrt{N_{ee}/N_{\mu\mu}}$ is a correction factor accounting for the differences in acceptance and efficiency for electrons and muons, measured using $Z/\gamma^* \to e^+e^-$ and $Z/\gamma^* \to \mu^+\mu^-$ events in data. An uncertainty of 70% in the estimated yield of the nonresonant backgrounds is included to account for the statistical and systematic uncertainties of the extrapolation from the $e^{\pm}\mu^{\mp}$ control region. A similar method using sideband regions of the Z bo-

son mass peak was used to estimate these backgrounds in the 8 TeV analysis, as described in Ref. [16]. The same method was used in the 13 TeV analysis as a cross-check and the differences between the results of the two methods of 10–15% are included as additional systematic uncertainties.

Additional uncertainties in the background estimates arise from lepton efficiencies, momentum scale, jet energy scale and resolution, and $E_{\mathrm{T}}^{\mathrm{miss}}$ energy scale and resolution, each contributing up to 2%. Statistical uncertainties are included for all simulated samples. These uncertainties are propagated as both shape and normalisation variations of the predicted m_{T} distributions.

The numbers of expected and observed events for the 0-jet and 1-jet categories in the 13 TeV analysis are given in Table 5. The signal yield assumes the SM ZH production rate for a Higgs boson with the mass of 125 GeV decaying to invisible particles with 100% branching fraction.

Table 5: Predicted signal and background yields and observed number of events after full selection in the 13 TeV analysis. The numbers are given for the 0-jet and 1-jet categories, separately for the e^+e^- and $\mu^+\mu^-$ final states. The uncertainties include statistical and systematic components. The signal prediction assumes a SM ZH production rate for a Higgs boson with the mass of 125 GeV and a 100% branching fraction to invisible particles.

Process	0 jets		1 jet	
	$\mu^+\mu^-$	e^+e^-	$\mu^+\mu^-$	e^+e^-
ZH, $m_{\mathrm{H}} = 125$ GeV	5.97 ± 0.55	4.27 ± 0.39	1.29 ± 0.20	0.98 ± 0.15
$Z(l^+l^-)$+jets	0.45 ± 0.45	0.30 ± 0.30	0.45 ± 0.45	0.30 ± 0.30
$ZZ \to llvv$	10.4 ± 1.14	7.46 ± 0.81	2.04 ± 0.31	1.49 ± 0.23
$WZ \to lvll$	3.42 ± 0.28	2.40 ± 0.19	1.04 ± 0.10	1.00 ± 0.10
Top/WW/$\tau\tau$	0.69 ± 0.23	0.88 ± 0.29	0.44 ± 0.22	0.26 ± 0.13
VVV	-	-	0.13 ± 0.06	0.07 ± 0.03
Total background	15.0 ± 1.28	11.0 ± 0.93	4.10 ± 0.60	3.12 ± 0.41
Data	18	8	5	1

4.3 The V(jj)-tagged and monojet analyses

Searches for final states with central jets and $E_{\mathrm{T}}^{\mathrm{miss}}$ suffer from large backgrounds. However, the ggH mode and the VH associated mode, in which the vector boson decays hadronically, have relatively large signal contributions despite the tight requirements on the jets. The search strategies for the V(jj)H and ggH modes are very similar, targeting events with large $E_{\mathrm{T}}^{\mathrm{miss}}$, with the missing transverse momentum vector, recoiling against jets from either quark/gluon radiation or a hadronically decaying vector boson. Events are categorised into two categories, depending on the jet properties. The dominant backgrounds arise from $Z(\nu\nu)$+jets and $W(l\nu)$+jets, accounting for 90% of the total background. These backgrounds are estimated using control regions in data and a simultaneous fit to the $E_{\mathrm{T}}^{\mathrm{miss}}$ distribution of the events across all regions is performed to extract a potential signal.

4.3.1 Event selection

The dataset is collected using a suite of triggers with requirements on $E_{\mathrm{T}}^{\mathrm{miss}}$ and hadronic activity. In the 8 TeV analysis two triggers are used: the first requires a $E_{\mathrm{T}}^{\mathrm{miss}} > 120$ GeV, while the second requires an $E_{\mathrm{T}}^{\mathrm{miss}}$ greater than 95 or 105 GeV, depending on the data taking period, together with a jet of $p_{\mathrm{T}} > 80$ GeV and $|\eta| < 2.6$. In the 13 TeV dataset, the trigger requires

$E_{\mathrm{T}}^{\mathrm{miss}} > 90\,\mathrm{GeV}$ and $H_{\mathrm{T}}^{\mathrm{miss}} > 90\,\mathrm{GeV}$, where $H_{\mathrm{T}}^{\mathrm{miss}}$ is defined as the magnitude of the vector sum of the transverse momenta of all jets with $p_{\mathrm{T}} > 20$ GeV. Additional selection requirements are imposed on the jets used in the $H_{\mathrm{T}}^{\mathrm{miss}}$ computation in order to remove events resulting from rare anomalous detector signals. In both 8 and 13 TeV datasets the calculation of $E_{\mathrm{T}}^{\mathrm{miss}}$ does not include muons, allowing for the same triggers to be used in the signal, single muon and dimuon control regions. For events selected for the analysis, the trigger efficiency is found to be greater than 99% (98%) at 8 (13) TeV.

Dedicated quality filters are applied for tracks, muons, and other physics objects to remove events with large misreconstructed $E_{\mathrm{T}}^{\mathrm{miss}}$. To reduce the QCD multijet background the events in the 8 TeV analysis are required to satisfy the requirement that the angle between the $\vec{p}_{\mathrm{T}}^{\mathrm{miss}}$ and the leading jet $\Delta\phi(\vec{p}_{\mathrm{T}}^{\mathrm{miss}}, \mathrm{j}) > 2$. In the 13 TeV data set the requirement is instead $\min\Delta\phi(\vec{p}_{\mathrm{T}}^{\mathrm{miss}}, \mathrm{j}) > 0.5$, where the minimum is over the four leading jets in the event.

Backgrounds from top quark decays are suppressed by applying a veto on events containing a b jet with $p_{\mathrm{T}} > 15$ GeV. Events in the signal regions of the 8 (13) TeV analysis are vetoed if they contain an electron or muon with $p_{\mathrm{T}} > 10$ GeV, a photon with $p_{\mathrm{T}} > 10\,(15)$ GeV, or a τ lepton with $p_{\mathrm{T}} > 18\,(15)$ GeV.

Selected events are classified by the topology of the jets in order to distinguish initial- or final-state radiation from hadronic vector boson decays. This results in two exclusive event categories, the monojet and V(jj)-tagged categories. If the vector boson decays hadronically and has sufficiently high transverse momentum, its hadronic decay products are captured by a single reconstructed large-radius jet. Events in the V(jj)-tagged category are required to have $E_{\mathrm{T}}^{\mathrm{miss}} > 250\,\mathrm{GeV}$ and contain a reconstructed $R = 0.8$ jet with $p_{\mathrm{T}} > 200\,(250)$ GeV and $|\eta| < 2.0$ (2.4) in the 8 (13) TeV analysis. Additional requirements are included to improve the vector boson jet purity by using the "subjettiness" quantity τ_2/τ_1, as defined in Refs. [67, 68], which identifies jets with a two sub-jet topology, and the pruned jet mass ($\mathrm{m_{prune}}$) [69]. The τ_2/τ_1 ratio is required to be smaller than 0.6 (0.5) and $\mathrm{m_{prune}}$ is required to be in the range 60–110 (65–105) GeV in the 8 (13) TeV analyses. The optimisation of the selection for VH production is performed independently for the 8 and 13TeV datasets.

If an event fails the V(jj)-tagged selection, it can instead be included in the monojet category. Events in the monojet category are required to contain at least one jet with $p_{\mathrm{T}} > 150\,(100)$ GeV and $|\eta| < 2.0\,(2.5)$ in the 8 (13) TeV analysis. In the 8 TeV analysis, events with additional jets are vetoed in both the V(jj)-tagged and monojet categories. The veto allows up to one additional jet provided that the separation of that jet from the leading jet in azimuthal angle satisfies $\Delta\phi < 2$. This veto was dropped for the 13 TeV analysis to increase the signal acceptance. Finally, events are required to have $E_{\mathrm{T}}^{\mathrm{miss}} > 200\,\mathrm{GeV}$.

A summary of the event selection for the V(jj)-tagged and monojet categories is given in Table 6 In addition to this selection, events that pass the corresponding VBF selection are vetoed to avoid an overlap with the VBF search.

4.3.2 Background estimation

The dominant $\mathrm{Z}(\nu\nu)$+jets and $\mathrm{W}(l\nu)$+jets backgrounds are estimated from control regions in data consisting of dimuon, single-muon, and γ+jets events. In the 13 TeV analysis, additional control regions, selecting dielectron and single-electron events are used. The $E_{\mathrm{T}}^{\mathrm{miss}}$ in each control region is redefined to mimic the $E_{\mathrm{T}}^{\mathrm{miss}}$ distribution of the $\mathrm{Z}(\nu\nu)$+jets and $\mathrm{W}(l\nu)$+jets backgrounds in the signal region by excluding the leptons or the photon from the computation of $E_{\mathrm{T}}^{\mathrm{miss}}$.

Table 6: Event selections for the V(jj)-tagged and monojet invisible Higgs boson decay searches using the 8 and 13 TeV data sets. The requirements on $p_{\mathrm{T}}^{\mathrm{j}}$ and $|\eta|^{\mathrm{j}}$ refer to the highest p_{T} (large-radius) jet in the monojet (V(jj)-tagged) events.

	8 TeV		13 TeV	
	V(jj)-tag	monojet	V(jj)-tag	monojet
$p_{\mathrm{T}}^{\mathrm{j}}$	> 200 GeV	> 150 GeV	> 250 GeV	> 100 GeV
$\lvert\eta\rvert^{\mathrm{j}}$	< 2		< 2.4	< 2.5
$E_{\mathrm{T}}^{\mathrm{miss}}$	> 250 GeV	> 200 GeV	> 250 GeV	> 200 GeV
τ_2/τ_1	< 0.5	–	< 0.6	–
$\mathrm{m_{prune}}$	60–110 GeV	–	65–105 GeV	-
$\mathrm{min}\Delta\phi(\vec{p}_{\mathrm{T}}^{\mathrm{miss}},\mathrm{j})$ [1]	> 2		> 0.5	
$\mathrm{N_j}$	$= 1$ [2]		-	

[1] The 8 TeV analysis only uses the leading jet for this selection.
[2] An additional jet is allowed only if it falls within $\Delta\phi < 2$ of the leading jet.

A dimuon control region is defined by selecting events that contain two opposite-sign muons with $p_{\mathrm{T}}^{\mu_1,\mu_2} > 10$ (20), 10 GeV at 8 (13) TeV and an invariant mass between 60 and 120 GeV. A single-muon control region is defined by selecting events with an isolated muon with $p_{\mathrm{T}} > 20$ GeV.

The γ+jets control sample is constructed using single-photon triggers. Events are required to have a well isolated photon with $p_{\mathrm{T}} > 170$ (175) GeV and $|\eta| < 2.5$ (1.44) in the 8 (13) TeV analysis to ensure a γ+jets purity of at least 95% [30].

A dielectron control region at 13 TeV is defined using similar requirements on the two electrons as for the dimuon control region. Single electron triggers with a p_{T} threshold of 27 GeV are used to select events, and at least one of the selected electrons is required to have $p_{\mathrm{T}} > 40$ GeV. Additionally a single-photon trigger with a p_{T} threshold of 165 GeV is used to recover events in which the p_{T} of the Z boson is large (more than 600 GeV), leading to inefficiencies of the isolation requirements. A single-electron control sample is selected using the same triggers. The p_{T} of the electron in this region is required to be greater than 40 GeV in order to reach the region in which the trigger is 100% efficient. An additional requirement of $E_{\mathrm{T}}^{\mathrm{miss}} > 50$ GeV is imposed on single-electron events in order to suppress the QCD background.

The events in all control regions are required to pass all of the selection requirements applied in the signal region, except for the lepton and photon vetos. In this case the $E_{\mathrm{T}}^{\mathrm{miss}}$ is defined excluding the leptons and photons used to select the events. As in the signal region, events in the control regions are separated into V(jj)-tagged and monojet categories.

The $E_{\mathrm{T}}^{\mathrm{miss}}$ distribution of the $\mathrm{Z}(\nu\nu)$+jets and $\mathrm{W}(l\nu)$+jets backgrounds is estimated from a maximum likelihood fit, performed simultaneously across all $E_{\mathrm{T}}^{\mathrm{miss}}$ bins in the signal and control regions. The expected number of $\mathrm{Z}(\nu\nu)$+jets (and $\mathrm{W}(l\nu)$+jets in the 8 TeV analysis) in each bin of $E_{\mathrm{T}}^{\mathrm{miss}}$ are free parameters of the fit. For each bin in $E_{\mathrm{T}}^{\mathrm{miss}}$, the ratio of the $\mathrm{Z}(\nu\nu)$+jets yield in the signal region to the corresponding yields of the $\mathrm{Z}(\mu^+\mu^-)$+jets, $\mathrm{Z}(\mathrm{e}^+\mathrm{e}^-)$+jets and γ+jets processes in the dimuon, dielectron, and γ+jets control regions are used to determine the expectations in these control regions for a given value of the free parameters [56]. Similarly, the ratio of the $\mathrm{W}(l\nu)$+jets yield in the signal region to the corresponding yields of the $\mathrm{W}(\mu\nu)$+jets and $\mathrm{W}(\mathrm{e}\nu)$+jets) processes in the single-muon and single-electron control regions are used to determine the expectations in the single-muon and single-electron control regions. The ratios are

determined from simulation after applying p_T-dependent NLO QCD K-factors derived using the MADGRAPH5_AMC@NLO MC generator and p_T-dependent NLO electroweak K-factors derived from theoretical calculations [70–73]. In the 8 TeV analysis, the ratio between the two backgrounds is left unconstrained in the fit. In the 13 TeV analysis, the ratio of $W(l\nu)$+jets to $Z(\nu\nu)$+jets in the signal region is constrained to that predicted in simulation after the application of NLO QCD and electroweak K-factors.

Systematic uncertainties are included to account for theoretical uncertainties in the γ to Z and W to Z differential cross section ratios due to the choice of the renormalisation and factorisation scales and PDF effects [74]. The value of the systematic uncertainty in these differential cross-sections due to higher order electroweak corrections is taken to be the full NLO electroweak correction, which can be as large as 20% for large values of E_T^{miss}. For the kinematic region in which the K-factors are applied, the interference between QCD and electroweak effects reduces the correction obtained compared to applying the K-factors independently. The difference between accounting for this interference or not is covered by the systematic uncertainties applied. Uncertainties in the selection efficiencies of muons, electrons, photons (up to 2%), and hadronically decaying τ leptons (3%) are included. The uncertainty in the modelling of E_T^{miss} in simulation is dominated by the jet energy scale uncertainty and varies between 2 and 5%, depending on the E_T^{miss} bin.

The remaining sub-dominant backgrounds due to top quark and diboson processes are estimated directly from simulation. Systematic uncertainties of 10% and 20% are assigned to the cross sections for the top quark [60] and diboson backgrounds [62, 63]. An additional 10% uncertainty is assigned to the top quark backgrounds to account for the discrepancies observed between data and the simulation in the p_T distribution of the $t\bar{t}$ pair. An inefficiency of the V(jj) tagging requirements can cause events to migrate between the V(jj)-tagged and monojet categories. An uncertainty in the V(jj) tagging of 13% is included to account for this. This uncertainty comprises a statistical component which is uncorrelated between the 8 and 13 TeV analyses and a systematic component which is fully correlated.

In the 8 TeV dataset, the contribution from QCD multijet events is determined using simulation normalised to the data while in the 13 TeV dataset the contribution is determined using a dedicated control sample. Although large uncertainties are included to account for the extrapolation from the control region to the signal region, the impact on the final results is small.

Figure 4 shows the distribution of E_T^{miss} in data for the V(jj)-tagged and monojet categories in the 13 TeV analysis and the background predicted after performing a simultaneous fit, which ignores the constraints from data in the signal regions. The signal expectation assuming SM rates for production of a Higgs boson with the mass of 125 GeV with $B(H \to inv.) = 100\%$ is superimposed.

5 Results

No significant deviations from the SM expectations are observed in any of the searches performed. The results are interpreted in terms of upper limits on $B(H \to inv.)$ under various assumptions about the Higgs boson production cross section. Limits are calculated using an asymptotic approximation of the CL_s prescription [75, 76] using a profile likelihood ratio test statistic [77], in which systematic uncertainties are modelled as nuisance parameters $\boldsymbol{\theta}$ following a frequentist approach [78].

The profile likelihood ratio is defined as,

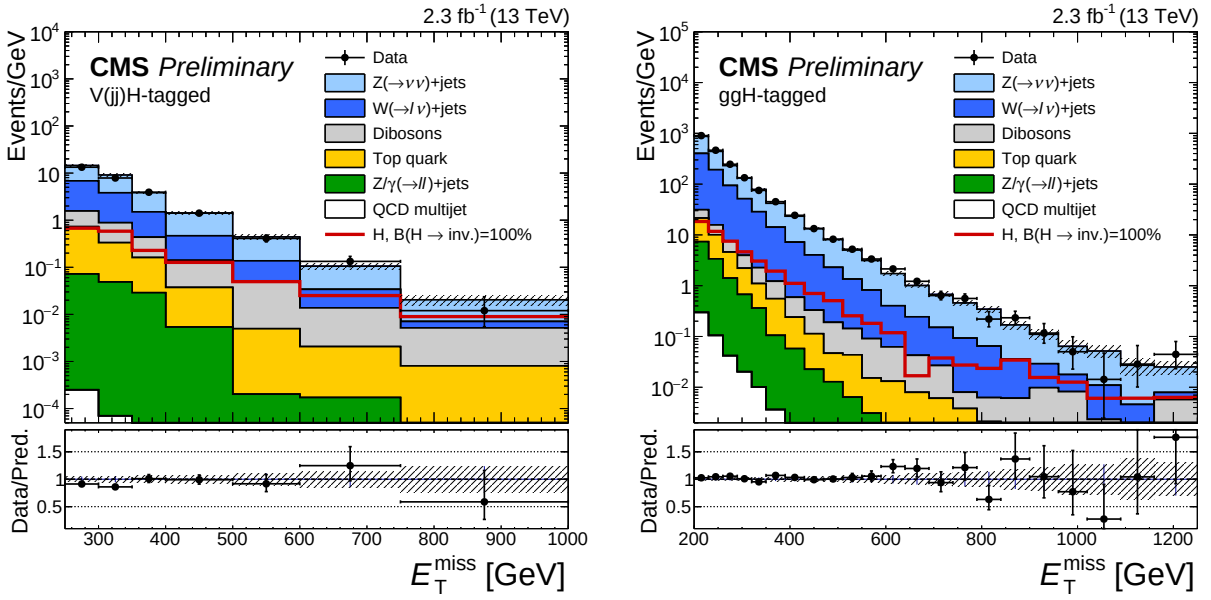

(a) (b)

Figure 4: Distributions of $E_{\mathrm{T}}^{\mathrm{miss}}$ in data and predicted background contributions in the (a) V(jj)-tagged and (b) monojet categories at 13 TeV. The background prediction is taken from a fit using only the control regions and the shaded bands represent the statistical and systematic uncertainties in the backgrounds after that fit. The horizontal bars on the data points represent the width of the bin centred at that point. The expectations from a Higgs boson with the mass of 125 GeV decaying to invisible particles with a branching fraction of 100% are superimposed.

$$\mathrm{q} = -2\ln\frac{L(\mathrm{data}|\mathrm{B}(\mathrm{H}\to\mathrm{inv.}),\hat{\hat{\boldsymbol{\theta}}})}{L(\mathrm{data}|\hat{\mathrm{B}}(\mathrm{H}\to\mathrm{inv.}),\hat{\boldsymbol{\theta}})},$$

where $\hat{\mathrm{B}}(\mathrm{H}\to\mathrm{inv.})$ represents the value of the Higgs boson branching fraction to invisible particles, which maximises the likelihood L for the observed data and $\hat{\boldsymbol{\theta}}$ and $\hat{\hat{\boldsymbol{\theta}}}$ denote the unconditional maximum likelihood estimates for the nuisance parameters and the estimates for a specific value of $\mathrm{B}(\mathrm{H}\to\mathrm{inv.})$. The value of $\mathrm{B}(\mathrm{H}\to\mathrm{inv.})$ is restricted to be positive when maximising the likelihood.

The statistical procedure accounts for correlations between the nuisance parameters in each of the analyses. The uncertainties in the diboson cross sections, the lepton efficiencies, momentum scales, and the integrated luminosity are correlated across all categories of a given dataset. The uncertainties in the inclusive signal cross sections are additionally correlated across the measurements at 7, 8, and 13 TeV.

The kinematics of the jets selected in the VBF category are distinct from those selected in the V(jj)-tagged and monojet categories. For this reason, the jet energy scale and resolution uncertainties are considered uncorrelated between those categories. The b jet energy scale and resolution uncertainties for the $\mathrm{Z}(\mathrm{b\bar{b}})$ category are estimated using a different technique from that used for other jets and so are treated as uncorrelated with other searches [79].

Where simulation is used to model the $E_{\mathrm{T}}^{\mathrm{miss}}$ distributions of the signal or backgrounds, uncertainties are propagated from the jet and lepton energy scales and resolutions as well as from

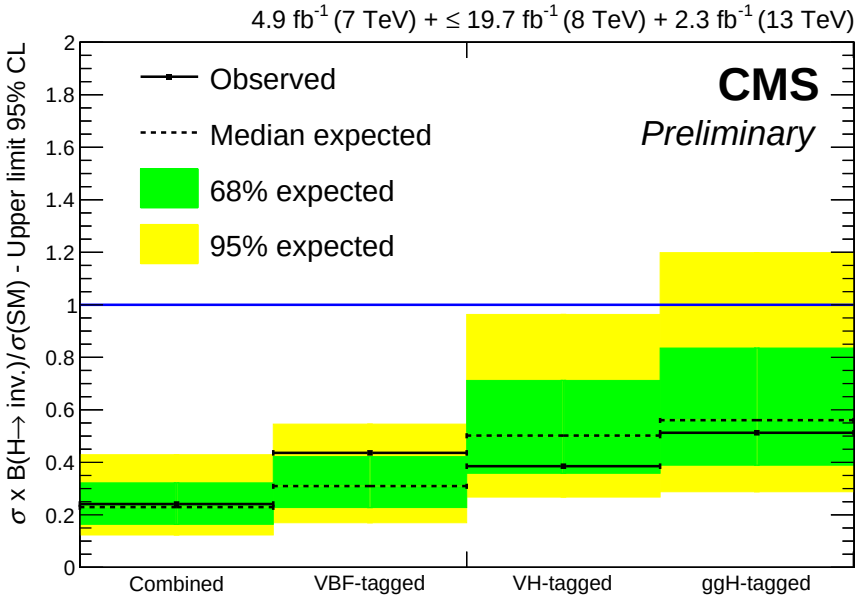

Figure 5: Observed and expected 95% CL limits on $\sigma \times \mathrm{B}(\mathrm{H} \to \mathrm{inv.})/\sigma(\mathrm{SM})$ for individual combinations of categories targeting qqH, VH, and ggH production, and the full combination assuming a Higgs boson with the mass of 125 GeV.

modelling of the unclustered energy. These uncertainties are treated as fully correlated between the 7, 8, and 13 TeV datasets, except for the 8 TeV V(jj)-tagged and monojet categories for which independent calibrations based on control samples in data are applied, as described in Section 4.3.2.

Systematic uncertainties in the inclusive ggH, qqH, and VH production cross sections due to scale and PDF choices are taken directly from Ref. [38] and treated as fully correlated across the 7, 8, and 13 TeV data sets. An additional systematic uncertainty of 50% in the ggH production cross section of the Higgs boson in association with two jets is included for the contribution of ggH in the VBF categories. This uncertainty is estimated by comparing the two-jet NLO generators POWHEG2.0+MINLO [80] and MADGRAPH5_AMC@NLO2.0. Furthermore, an uncertainty in the Higgs boson p_{T} distribution in ggH production is included in the monojet categories and estimated by varying the renormalisation and factorisation scales [81]. This uncertainty is correlated between the 8 and 13 TeV categories. Uncertainties in the acceptance from PDF effects are evaluated independently for the different signal processes in each category and treated as additional normalization nuisance parameters.

Observed and expected upper limits on $\sigma \times \mathrm{B}(\mathrm{H} \to \mathrm{inv.})/\sigma(\mathrm{SM})$ are determined at a 95% CL and presented in Fig. 5. The limits are obtained from the combination of all categories and from sub-combinations of categories, which target one of the ggH, qqH, and VH production mechanisms, corresponding to the analysis tags in Table 1. The relative contributions from the different production mechanisms in these results are fixed to their SM predictions within the uncertainties. Assuming SM production rates for ggH, qqH, and VH processes, the combination yields an observed (expected) upper limit of $\mathrm{B}(\mathrm{H} \to \mathrm{inv.}) < 0.24\ (0.23)$ at a 95% CL.

The profile likelihood ratio as a function of $\mathrm{B}(\mathrm{H} \to \mathrm{inv.})$ using partial combinations of the 7+8 and 13 TeV analyses, and for the full combination are shown in Fig. 6(a). The profile likelihood ratio scans for the partial combinations of the VBF-tagged, VH-tagged, and ggH-tagged anal-

yses are shown in Fig. 6(b). The results are shown for the observed data and for an Asimov dataset [77] in which $B(H \to \text{inv.}) = 0$ is assumed.

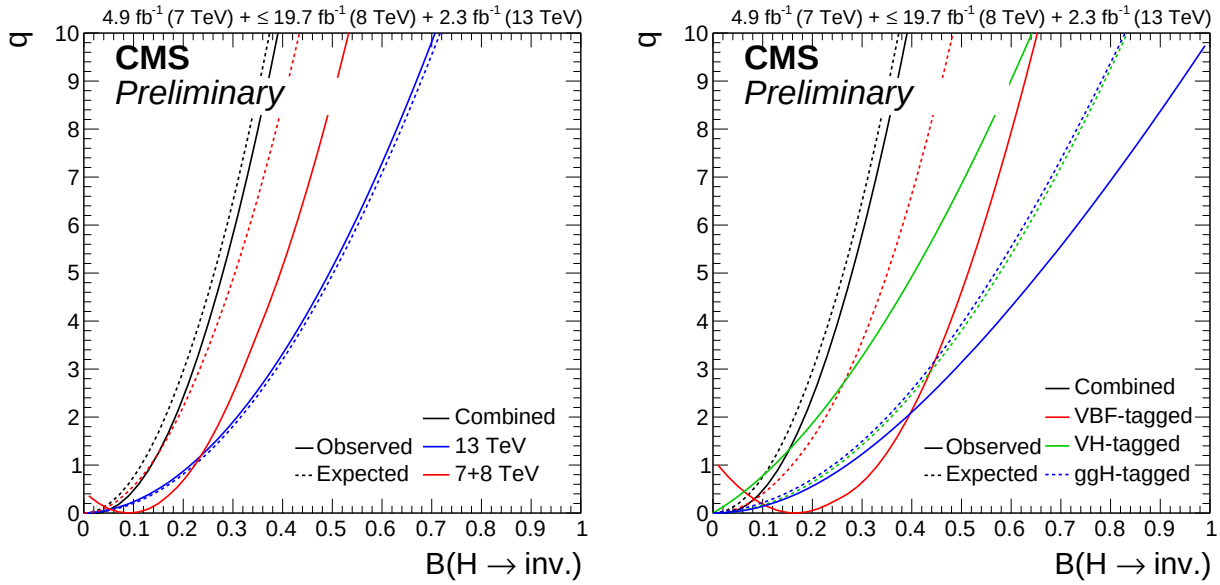

(a) (b)

Figure 6: Profile likelihood ratio as a function of $B(H \to \text{inv.})$ assuming SM production cross selections of a Higgs boson with the mass of 125 GeV. The solid curves represent the observation in data and the dashed curves represents the expected result assuming no invisible decays of the Higgs boson. (a) The observed and expected likelihood scans for the partial combinations of the 7+8 and 13 TeV analyses, and the full combination. (b) The observed and expected likelihood scans for the partial combinations of the VBF-tagged, VH-tagged, and ggH-tagged analyses, and the full combination.

The dominant systematic uncertainties for the VBF-tagged, $Z(l^+l^-)$-tagged, V(jj)-tagged, and ggH-tagged searches in the 13 TeV data set are listed in Tables 7, 8, 9 and, 10. The impact of each independent source of systematic uncertainty is calculated as the maximum difference in the fitted value of $B(H \to \text{inv.})$, for an Asimov data set in which $B(H \to \text{inv.})$ is assumed to be 100%, when varying the nuisance parameter associated to that source of systematic uncertainty within one standard deviation of its maximum likelihood estimate value. The total uncertainty, fixing all nuisance parameters associated to systematic uncertainties that are not expected to improve with additional luminosity, for each analysis is also shown. Finally, the total uncertainty is given for each analysis.

Table 7: Dominant sources of systematic uncertainties and their impact on the fitted value of B(H $\rightarrow$ inv.) in the VBF-tagged analysis with the 13 TeV data. The systematic uncertainties are split into common uncertainties and those specific to the signal model. The total expected uncertainty and the total uncertainty fixing all constrained nuisance parameters to their maximum likelihood estimates (statistical only) are also given.

Systematic uncertainty	Impact
Common	
W to Z ratio in QCD produced V+jets	13%
W to Z ratio in EW produced V+jets	6.3%
Jet energy scale+resolution	6.0%
QCD multijet normalisation	4.3%
PU mis-modelling	4.2%
Lepton efficiencies	2.5%
Luminosity	2.2%
Signal specific	
ggH acceptance	3.8%
QCD scale + PDF (qqH)	1.8%
QCD scale + PDF (ggH)	$< 0.2\%$
Total statistical only	$-27/+28\%$
Total uncertainty	$-33/+32\%$

Table 8: Dominant sources of systematic uncertainties and their impact on the fitted value of B(H $\rightarrow$ inv.) in the Z(l^+l^-)-tagged analysis with the 13 TeV data. The systematic uncertainties are split into common uncertainties and those specific to the signal model. The total expected uncertainty and the total uncertainty fixing all constrained nuisance parameters to their maximum likelihood estimates (statistical only) are also given.

Systematic uncertainty	Impact
Common	
ZZ background theory	16%
luminosity	8.4%
b jet tag efficiency	6.2%
Electron efficiency	6.2%
Muon efficiency	6.2%
Electron energy scale	3.2%
Muon momentum scale	3.2%
Jet energy scale	2.2%
Diboson normalisation	5.3%
eμ region extrapolation	4.0%
Z(l^+l^-)normalisation	4.8%
Signal specific	
QCD scale + PDF (qqZH)	7.4%
QCD scale + PDF (ggZH)	4.0%
Total statistical only	$-50/+56\%$
Total uncertainty	$-55/+62\%$

Table 9: Dominant sources of systematic uncertainties and their impact on the fitted value of $B(H \to \text{inv.})$ in the V(jj)-tagged analysis with the 13 TeV data. The systematic uncertainties are split into common uncertainties and those specific to the signal model. The total expected uncertainty and the total uncertainty fixing all constrained nuisance parameters to their maximum likelihood estimates (statistical only) are also given.

Systematic uncertainty	Impact
Common	
γ+jets/Z($\nu\nu$)+jets ratio theory	32%
W($l\nu$)+jets/Z($\nu\nu$)+jets ratio theory	21%
Jet energy scale+resolution	12%
V-tagging efficiency	12%
Lepton veto efficiency	13%
Electron efficiency	13%
Muon efficiency	8.6%
b jet tag efficiency	5.7%
Photon efficiency	3.1%
$E_{\mathrm{T}}^{\mathrm{miss}}$ scale	4.6%
Top quark background normalisation	6.0%
Diboson background normalisation	$< 1\%$
Luminosity	$< 1\%$
Signal specific	
ggH p_{T}-spectrum	12%
QCD scale + PDF (ggH)	3.0%
QCD scale + PDF (VH)	1.4%
Total statistical only	$-46/+50\%$
Total uncertainty	$-69/+74\%$

By varying the assumed SM production rates, the relative sensitivity of the different categories to an invisible Higgs signal is studied. The rates for ggH, qqH, and VH production can be expressed in terms of the relative coupling modifiers κ_F and κ_V that scale the couplings of the Higgs boson to the SM fermions and vector bosons, respectively [82]. In this formalism, the total width of the Higgs boson is the sum of the partial widths to the visible channels, determined as a function of κ_V and κ_F, and an invisible decay width. The contribution from ggZH is scaled to account for the interference between the tH and ZH diagrams. The background from VH($H \to b\bar{b}$) in the Z($b\bar{b}$) search is scaled consistently with the other search channels. The SM production rates are recovered for $\kappa_F = \kappa_V = 1$. Figure 7 shows a 95% CL upper limits on $B(H \to \text{inv.})$ obtained as a function of κ_F and κ_V. The 68% and 95% CL limits for κ_F, κ_V from Ref. [4] are superimposed. The observed upper limit on $B(H \to \text{inv.})$ varies between 0.2 and 0.3 at a 95% CL within the 95% confidence region shown.

5.1 Higgs-portal models

The upper limit on $B(H \to \text{inv.})$, under the assumption of SM production cross sections for the Higgs boson, can be interpreted in the context of a Higgs-portal model of DM interactions. In these models, a hidden sector provides a stable DM particle candidate with direct couplings to the SM Higgs sector. Direct detection experiments are sensitive to elastic interactions between DM particles and nuclei via Higgs boson exchange. These interactions produce nuclear recoil signatures, which can be interpreted in terms of a DM-nucleon interaction cross section. The sensitivity varies as a function of the DM particle mass, with relatively small DM masses being

Table 10: Dominant sources of systematic uncertainties and their impact on the fitted value of $B(H \to \text{inv.})$ in the ggH-tagged analysis with the 13 TeV data. The systematic uncertainties are split into common uncertainties and those specific to the signal model. The total expected uncertainty and the total uncertainty fixing all constrained nuisance parameters to their maximum likelihood estimates (statistical only) are also given.

Systematic uncertainty	Impact
Common	
Muon efficiency	24%
Electron efficiency	22%
Lepton veto efficiency	16%
b jet tag efficiency	3.2%
$W(l\nu)$+jets/$Z(\nu\nu)$+jets ratio theory	16%
γ+jets/$Z(\nu\nu)$+jets ratio theory	5.8%
Jet energy scale+resolution	10%
E_T^{miss} scale	1.8%
Luminosity	3.0%
Diboson background normalisation	2.7%
Top quark background normalisation	$< 1\%$
Signal specific	
ggH p_T-spectrum	15%
QCD scale + PDF (ggH)	5.8%
Total statistical only	$-22/+25\%$
Total uncertainty	$-55/+62\%$

harder to probe. If the DM mass is smaller than $m_H/2$, the invisible Higgs decay width, $\Gamma_{inv.}$, can be translated into the spin-independent DM-nucleon elastic cross section, assuming either a scalar or fermion DM candidate. This translation is performed using the procedures outlined in Ref. [10] and using the relation $B(H \to \text{inv.}) = \Gamma_{inv.}/(\Gamma_{SM} + \Gamma_{inv.})$, where $\Gamma_{SM} = 4.07\,\text{MeV}$ [82]. Figure 8 shows the upper 90% CL upper limits on the spin-independent DM-nucleon cross section as a function of the DM mass, assuming $m_H = 125\,\text{GeV}$, for the scalar and fermion DM scenarios. In Ref. [10], the dimensionless quantity f_N parameterizes the Higgs-nucleon coupling. The central values for the exclusion limits are derived assuming $f_N = 0.326$, taken from Ref. [83], while alternative values of 0.260 and 0.629 are taken from the MILC Collaboration [84]. The limits are compared to those from from the LUX [85] and CDMSlite [86] experiments, which provide the strongest direct constraints on the spin-independent DM-nucleon cross section in the range of DM particle masses probed by this analysis. The present CMS results provide more stringent limits for DM masses below 30 or 5 GeV, assuming a fermion or scalar DM particle, respectively.

6 Conclusions

A combination of searches for a Higgs boson decaying to invisible particles using Run 1 and Run 2 data sets has been presented. The combination includes searches targeting Higgs production in the ZH mode, in which a Z boson decays to l^+l^- or $b\bar{b}$, and the qqH mode which is the most sensitive channel. The combination also includes the first searches at CMS targeting VH production, in which the vector boson decays hadronically, and the ggH mode in which the Higgs boson is produced in association with jets. No significant deviations from the SM predctions are observed and upper limits are placed on the branching fraction for the Higgs boson

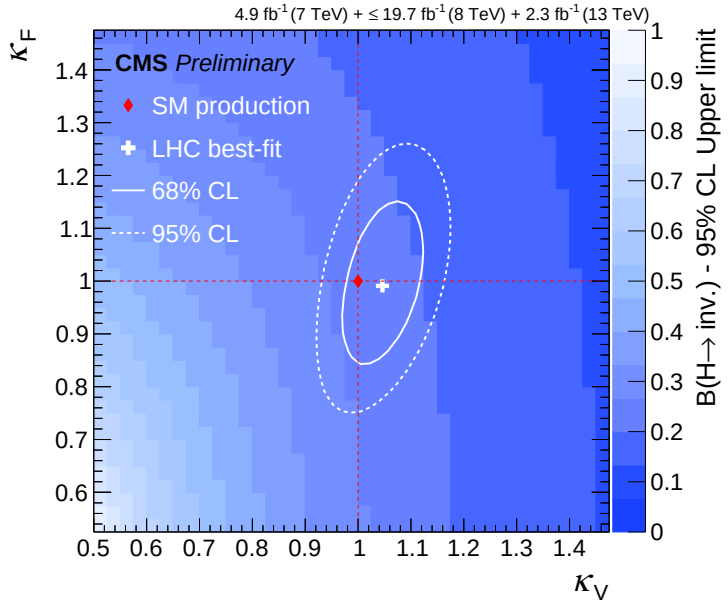

(a)

Figure 7: Observed 95% CL upper limits on $B(H \to \text{inv.})$ assuming a Higgs boson with the mass of 125 GeV whose production cross sections are scaled, relative to their SM values as a function of the coupling modifiers κ_F, κ_V. The 68% and 95% confidence regions for κ_F, κ_V from Ref. [4] are superimposed as the solid and dashed white contours, respectively. The SM prediction (red diamond) corresponds to $\kappa_F = \kappa_V = 1$.

decay to invisible particles. The combination of all searches yields an observed (expected) upper limit on $B(H \to \text{inv.})$ of 0.24 (0.23) at a 95% confidence level, assuming SM production of a Higgs boson with the mass of 125 GeV. The combined 90% CL limit of $B(H \to \text{inv.}) < 0.20$ has been interpreted in Higgs-portal models and constraints are placed on the spin-independent DM-nucleon interaction cross section. These limits provide stronger constraints than those from direct detection experiments for DM masses below 30 or 5 GeV, assuming a fermion or scalar DM particle, respectively.

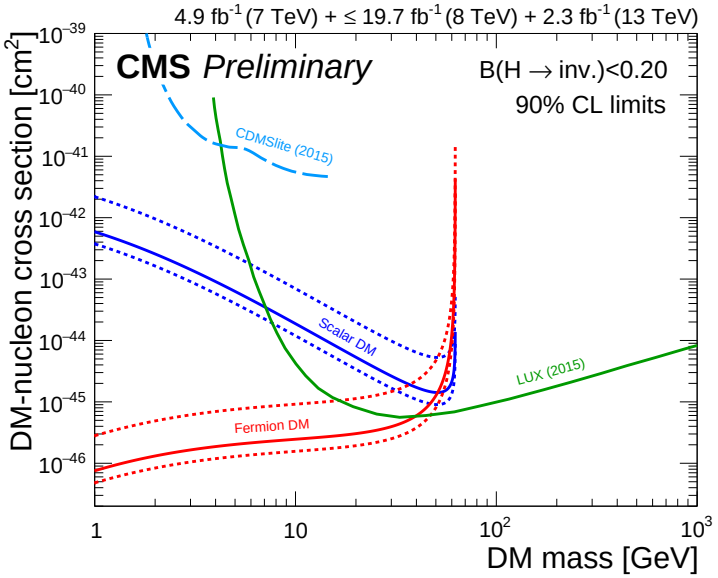

(a)

Figure 8: Limits on the spin-independent DM-nucleon scattering cross section in Higgs-portal models assuming a scalar or fermion DM particle. The dashed lines show the variation in the exclusion using alternative values for f_N as described in the text. The limits are given at the 90% CL to allow for comparison to direct detection constraints from the LUX [85] and CDMSlite [86] experiments.

References

[1] ATLAS Collaboration, "Observation of a new particle in the search for the Standard Model Higgs boson with the ATLAS detector at the LHC", *Phys. Lett. B* **716** (2012) 1, doi:10.1016/j.physletb.2012.08.020, arXiv:1207.7214.

[2] CMS Collaboration, "Observation of a new boson at a mass of 125 GeV with the CMS experiment at the LHC", *Phys. Lett. B* **716** (2012) 30, doi:10.1016/j.physletb.2012.08.021, arXiv:1207.7235.

[3] CMS Collaboration, "Observation of a new boson with mass near 125 GeV in pp collisions at $\sqrt{s}$ = 7 and 8 TeV", *JHEP* **06** (2013) 081, doi:10.1007/JHEP06(2013)081, arXiv:1303.4571.

[4] ATLAS, CMS Collaboration, "Measurements of the Higgs boson production and decay rates and constraints on its couplings from a combined ATLAS and CMS analysis of the LHC pp collision data at $\sqrt{s} = 7$ and 8 TeV", (2016). arXiv:1606.02266. Submitted to *JHEP*.

[5] G. Belanger et al., "The MSSM invisible Higgs in the light of dark matter and g-2", *Phys. Lett. B* **519** (2001) 93, doi:10.1016/S0370-2693(01)00976-5, arXiv:hep-ph/0106275.

[6] G. F. Giudice, R. Rattazzi, and J. D. Wells, "Graviscalars from higher dimensional metrics and curvature Higgs mixing", *Nucl. Phys. B* **595** (2001) 250, doi:10.1016/S0550-3213(00)00686-6, arXiv:hep-ph/0002178.

[7] M. Battaglia, D. Dominici, J. F. Gunion, and J. D. Wells, "The Invisible Higgs decay width in the add model at the LHC", in *Physics at TeV colliders. Proceedings*. 2004. arXiv:hep-ph/0402062.

[8] K. Y. Lee, Y. G. Kim, and S. Shin, "Singlet fermionic dark matter as a natural higgs portal model", in *Proceedings, 16th International Conference on Supersymmetry and the Unification of Fundamental Interactions (SUSY08)*. 2008. arXiv:0809.2745.

[9] S. Baek, P. Ko, W.-I. Park, and E. Senaha, "Higgs Portal Vector Dark Matter : Revisited", *JHEP* **05** (2013) 036, doi:10.1007/JHEP05(2013)036, arXiv:1212.2131.

[10] A. Djouadi, O. Lebedev, Y. Mambrini, and J. Quevillon, "Implications of LHC searches for Higgs–portal dark matter", *Phys. Lett. B* **709** (2012) 65, doi:10.1016/j.physletb.2012.01.062, arXiv:1112.3299.

[11] A. Djouadi, A. Falkowski, Y. Mambrini, and J. Quevillon, "Direct Detection of Higgs-Portal Dark Matter at the LHC", *Eur. Phys. J. C* **73** (2013) 2455, doi:10.1140/epjc/s10052-013-2455-1, arXiv:1205.3169.

[12] G. Servant and S. Tulin, "Baryogenesis and Dark Matter through a Higgs Asymmetry", *Phys. Rev. Lett.* **111** (2013) 151601, doi:10.1103/PhysRevLett.111.151601, arXiv:1304.3464.

[13] T. Cohen, D. E. Morrissey, and A. Pierce, "Electroweak Baryogenesis and Higgs Signatures", *Phys. Rev. D* **86** (2012) 013009, doi:10.1103/PhysRevD.86.013009, arXiv:1203.2924.

[14] ATLAS Collaboration, "Search for Invisible Decays of a Higgs Boson Produced in Association with a Z Boson in ATLAS", *Phys. Rev. Lett.* **112** (2014) 201802, doi:10.1103/PhysRevLett.112.201802, arXiv:1402.3244.

[15] ATLAS Collaboration, "Search for invisible decays of the Higgs boson produced in association with a hadronically decaying vector boson in pp collisions at $\sqrt{s}$ = 8 TeV with the ATLAS detector", *Eur. Phys. J. C* **75** (2015) 337, doi:10.1140/epjc/s10052-015-3551-1, arXiv:1504.04324.

[16] CMS Collaboration, "Search for invisible decays of Higgs bosons in the vector boson fusion and associated ZH production modes", *Eur. Phys. J. C* **74** (2014) doi:10.1140/epjc/s10052-014-2980-6, arXiv:1404.1344.

[17] ATLAS Collaboration, "Search for invisible decays of a Higgs boson using vector-boson fusion in pp collisions at $\sqrt{s} = 8$ TeV with the ATLAS detector", *JHEP* **01** (2016) 172, doi:10.1007/JHEP01(2016)172, arXiv:1508.07869.

[18] ATLAS Collaboration, "Search for new phenomena in final states with an energetic jet and large missing transverse momentum in pp collisions at $\sqrt{s}$ =8 TeV with the ATLAS detector", *Eur. Phys. J. C* **75** (2015) 299, doi:10.1140/epjc/s10052-015-3517-3, 10.1140/epjc/s10052-015-3639-7, arXiv:1502.01518. [Erratum: *Eur. Phys. J. C* **75** (2015) 408].

[19] ATLAS Collaboration, "Constraints on new phenomena via Higgs boson couplings and invisible decays with the ATLAS detector", *JHEP* **11** (2015) 206, doi:10.1007/JHEP11(2015)206, arXiv:1509.00672.

[20] CMS Collaboration, "Particle-flow event reconstruction in CMS and performance for jets, taus, and MET", CMS Physics Analysis Summary CMS-PAS-PFT-09-001, 2009. Geneva, 2009.

[21] CMS Collaboration, "Commissioning of the Particle-flow event reconstruction with the first LHC collisions recorded in the CMS detector", CMS Physics Analysis Summary CMS-PAS-PFT-10-001, 2010, 2015.

[22] M. Cacciari, G. P. Salam, and G. Soyez, "The anti-k_t jet clustering algorithm", *JHEP* **04** (2008) 063, arXiv:0802.1189.

[23] CMS Collaboration, "Identification of b quark jets with the CMS experiment", *JINST* **8** (2013) doi:10.1088/1748-0221/8/04/P04013, arXiv:1211.4462.

[24] CMS Collaboration, "Performance of b tagging at $\sqrt{s}$=8 TeV in multijet, ttbar and boosted topology events", CMS Physics Analysis Summary CMS-PAS-BTV-13-001, CERN, Geneva, 2013.

[25] CMS Collaboration, "Identification of b quark jets at the CMS Experiment in the LHC Run 2", CMS Physics Analysis Summary CMS-PAS-BTV-15-001, CERN, Geneva, 2016.

[26] M. Cacciari, G. P. Salam, and G. Soyez, "FastJet user manual", *Eur. Phys. J. C* **72** (2012) 1896, doi:10.1140/epjc/s10052-012-1896-2, arXiv:1111.6097.

[27] CMS Collaboration, "Jet energy scale and resolution in the CMS experiment in pp collisions at 8 TeV", arXiv:1607.03663. Submitted to *JINST*.

[28] CMS Collaboration, "Determination of jet energy calibration and transverse momentum resolution in CMS", *JINST* **6** (2011) P11002, doi:10.1088/1748-0221/6/11/P11002, arXiv:1107.4277.

[29] CMS Collaboration, "Performance of electron reconstruction and selection with the CMS Detector in proton-proton collisions at $\sqrt{s}$= 8 TeV", *JINST* **10** (2015) P06005, doi:10.1088/1748-0221/10/06/P06005, arXiv:1502.02701.

[30] CMS Collaboration, "Performance of photon reconstruction and identification with the CMS detector in proton-proton collisions at $\sqrt{s}$ = 8 TeV", *JINST* **10** (2015) P08010, doi:10.1088/1748-0221/10/08/P08010, arXiv:1502.02702.

[31] CMS Collaboration, "The performance of the CMS muon detector in proton-proton collisions at $\sqrt{s} = 7$ TeV at the LHC", *JINST* **8** (2013) P11002, doi:10.1088/1748-0221/8/11/P11002, arXiv:1306.6905.

[32] M. Cacciari and G. P. Salam, "Pileup subtraction using jet areas", *Phys. Lett. B* **659** (2008) 119, doi:10.1016/j.physletb.2007.09.077, arXiv:0707.1378.

[33] CMS Collaboration, "Reconstruction and identification of τ lepton decays to hadrons and ν_τ at CMS", *JINST* **11** (2016) P01019, doi:10.1088/1748-0221/11/01/P01019, arXiv:1510.07488.

[34] CMS Collaboration, "Absolute calibration of the luminosity measurement at CMS: winter 2012 update", CMS Physics Analysis Summary CMS-PAS-SMP-12-008, CERN, Geneva, 2012.

[35] CMS Collaboration, "CMS luminosity based on pixel cluster counting - summer 2013 update", CMS Physics Analysis Summary CMS-PAS-LUM-13-001, CERN, Geneva, 2013.

[36] CMS Collaboration, "CMS luminosity measurement for the 2015 data taking period", CMS Physics Analysis Summary CMS-PAS-LUM-15-001, CERN, Geneva, 2015.

[37] ATLAS, CMS Collaboration, "Combined measurement of the higgs boson mass in pp collisions at $\sqrt{s} = 7$ and 8 TeV with the ATLAS and CMS experiments", *Phys. Rev. Lett.* **114** (2015) 191803, doi:10.1103/PhysRevLett.114.191803, arXiv:1503.07589.

[38] LHC Higgs Cross Section Working Group Collaboration, "Production cross sections and decay BRs for RUN-2". https://twiki.cern.ch/twiki/bin/view/LHCPhysics/LHCHXSWG.

[39] S. Alioli, P. Nason, C. Oleari, and E. Re, "A general framework for implementing NLO calculations in shower Monte Carlo programs: the POWHEG BOX", *JHEP* **06** (2010) 043, doi:10.1007/JHEP06(2010)043, arXiv:1002.2581.

[40] P. Nason and C. Oleari, "NLO Higgs boson production via vector-boson fusion matched with shower in POWHEG", *JHEP* **02** (2010) 037, doi:10.1007/JHEP02(2010)037, arXiv:0911.5299.

[41] S. Alioli, P. Nason, C. Oleari, and E. Re, "NLO Higgs boson production via gluon fusion matched with shower in POWHEG", *JHEP* **04** (2009) 002, doi:10.1088/1126-6708/2009/04/002, arXiv:0812.0578.

[42] T. Sjostrand, S. Mrenna, and P. Z. Skands, "PYTHIA 6.4 Physics and Manual", *JHEP* **05** (2006) 026, doi:10.1088/1126-6708/2006/05/026, arXiv:hep-ph/0603175.

[43] T. Sjostrand, S. Mrenna, and P. Z. Skands, "A Brief Introduction to PYTHIA 8.1", *Comput. Phys. Commun.* **178** (2008) 852, doi:10.1016/j.cpc.2008.01.036, arXiv:0710.3820.

[44] C. Anastasiou et al., "Higgs boson gluonfusion production at threshold in N^3LO QCD", *Phys. Lett. B* **737** (2014) 325, doi:10.1016/j.physletb.2014.08.067, arXiv:1403.4616.

[45] LHC Higgs Cross Section Working Group Collaboration, "Handbook of LHC Higgs Cross Sections: 3. Higgs Properties: Report of the LHC Higgs Cross Section Working Group", Technical Report arXiv:1307.1347. CERN-2013-004, Geneva, 2013.

[46] D. de Florian, G. Ferrera, M. Grazzini, and D. Tommasini, "Higgs boson production at the LHC: transverse momentum resummation effects in the $H \to 2\gamma$, $H \to WW \to lvlv$ and $H \to ZZ \to 4l$ decay modes", *JHEP* **06** (2012) 132, doi:10.1007/JHEP06(2012)132, arXiv:1203.6321.

[47] M. Grazzini and H. Sargsyan, "Heavy-quark mass effects in Higgs boson production at the LHC", *JHEP* **09** (2013) 129, doi:10.1007/JHEP09(2013)129, arXiv:1306.4581.

[48] J. Alwall et al., "MadGraph 5: going beyond", *JHEP* **06** (2011) 128, doi:10.1007/JHEP06(2011)128, arXiv:1106.0522.

[49] J. Alwall et al., "The automated computation of tree-level and next-to-leading order differential cross sections, and their matching to parton shower simulations", *JHEP* **07** (2014) 079, doi:10.1007/JHEP07(2014)079, arXiv:1405.0301.

[50] S. Alioli, P. Nason, C. Oleari, and E. Re, "NLO single-top production matched with shower in POWHEG: s- and t-channel contributions", *JHEP* **09** (2009) 111, doi:10.1007/JHEP02(2010)011, 10.1088/1126-6708/2009/09/111, arXiv:0907.4076. [Erratum: *JHEP* **02** (2010) 011].

[51] J. Pumplin et al., "New generation of parton distributions with uncertainties from global QCD analysis", *JHEP* **07** (2002) 012, doi:10.1088/1126-6708/2002/07/012, arXiv:hep-ph/0201195.

[52] R. D. Ball et al., "Impact of Heavy Quark Masses on Parton Distributions and LHC Phenomenology", *Nucl. Phys. B* **849** (2011) 296, doi:10.1016/j.nuclphysb.2011.03.021, arXiv:1101.1300.

[53] CMS Collaboration, "Study of the underlying event at forward rapidity in pp collisions at $\sqrt{s} = 0.9$, 2.76, and 7 TeV", *JHEP* **04** (2013) 072, doi:10.1007/JHEP04(2013)072, arXiv:1302.2394.

[54] CMS Collaboration, "Event generator tunes obtained from underlying event and multiparton scattering measurements", *Eur. Phys. J. C* **76** (2016) 155, doi:10.1140/epjc/s10052-016-3988-x, arXiv:1512.00815.

[55] GEANT4 Collaboration, "GEANT4: A Simulation toolkit", *Nucl. Instrum. Meth. A* **506** (2003) 250, doi:10.1016/S0168-9002(03)01368-8.

[56] CMS Collaboration, "Search for New Physics in the V/jet + MET final state", CMS Physics Analysis Summary CMS-PAS-EXO-12-055, Geneva, 2015.

[57] CMS Collaboration, "Data parking and data scouting at the CMS experiment", CMS Physics Analysis Summary CMS-DP-2012-022, CERN, Geneva, 2012.

[58] CMS Collaboration, "Measurement of the $pp \to ZZ$ production cross section and constraints on anomalous triple gauge couplings in four-lepton final states at $\sqrt{s}$ =8 TeV", *Phys. Lett. B* **740** (2015) 250, doi:10.1016/j.physletb.2014.11.059, arXiv:1406.0113.

[59] CMS Collaboration, "Measurement of the W^+W^- cross section in pp collisions at $\sqrt{s}$ = 8 TeV and limits on anomalous gauge couplings", arXiv:1507.03268. Submitted to *Eur. Phys. J. C*.

[60] CMS Collaboration, "Measurement of the top quark pair production cross section in proton-proton collisions at $\sqrt{s} = 13$ TeV", *Phys. Rev. Lett.* **116** (2016) 052002, doi:10.1103/PhysRevLett.116.052002, arXiv:1510.05302.

[61] CMS Collaboration, "Measurement of W^+W^- and ZZ production cross sections in pp collisions at $\sqrt{s} = 8$ TeV", *Phys. Lett. B* **721** (2013) 190, doi:10.1016/j.physletb.2013.03.027, arXiv:1301.4698.

[62] CMS Collaboration, "Measurement of the ZZ production cross section and Z $\to \ell\ell\ell'\ell'$ branching fraction in pp collisions at $\sqrt{s} = 13$ TeV", CMS Physics Analysis Summary CMS-PAS-SMP-16-001, Geneva, 2016.

[63] CMS Collaboration, "Measurement of the WZ production cross section in pp collisions at sqrt(s) = 13 TeV", CMS Physics Analysis Summary CMS-PAS-SMP-16-002, Geneva, 2016.

[64] K. Arnold et al., "VBFNLO: A Parton Level Monte Carlo for Processes with Electroweak Bosons – Manual for Version 2.5.0", arXiv:1107.4038.

[65] J. Baglio et al., "Release Note - VBFNLO 2.7.0", arXiv:1404.3940.

[66] J. M. Campbell, R. K. Ellis, and C. Williams, "Vector boson pair production at the LHC", *JHEP* **07** (2011) 018, doi:10.1007/JHEP07(2011)018, arXiv:1105.0020.

[67] J. Thaler and K. Van Tilburg, "Identifying boosted objects with N-subjettiness", *JHEP* **03** (2011) 015, arXiv:1011.2268.

[68] J. Thaler and K. Van Tilburg, "Maximizing boosted top identification by minimizing N-subjettiness", *JHEP* **02** (2012) 093, doi:10.1007/JHEP02(2012)093, arXiv:1108.2701.

[69] S. D. Ellis, C. K. Vermilion, and J. R. Walsh, "Recombination Algorithms and Jet Substructure: Pruning as a Tool for Heavy Particle Searches", *Phys. Rev. D* **81** (2010) 094023, arXiv:0912.0033.

[70] J. H. Kuhn, A. Kulesza, S. Pozzorini, and M. Schulze, "Electroweak corrections to hadronic photon production at large transverse momenta", *JHEP* **03** (2006) 059, doi:10.1088/1126-6708/2006/03/059, arXiv:hep-ph/0508253.

[71] S. Kallweit et al., "NLO electroweak automation and precise predictions for W+multijet production at the LHC", *JHEP* **04** (2015) 012, doi:10.1007/JHEP04(2015)012, arXiv:1412.5157.

[72] S. Kallweit et al., "NLO QCD+EW automation and precise predictions for V+multijet production", in *50th Rencontres de Moriond on QCD and High Energy Interactions La Thuile, Italy, March 21-28, 2015*. 2015. arXiv:1505.05704.

[73] S. Kallweit et al., "NLO QCD+EW predictions for V + jets including off-shell vector-boson decays and multijet merging", *JHEP* **04** (2016) 021, doi:10.1007/JHEP04(2016)021, arXiv:1511.08692.

[74] NNPDF Collaboration, "Parton distributions for the LHC Run II", *JHEP* **04** (2015) 040, doi:10.1007/JHEP04(2015)040, arXiv:1410.8849.

[75] T. Junk, "Confidence level computation for combining searches with small statistics", *Nucl. Instrum. Meth. A* **434** (1999) 435, doi:10.1016/S0168-9002(99)00498-2, arXiv:hep-ex/9902006.

[76] A. L. Read, "Presentation of search results: the CLs technique", *J. Phys. G* **28** (2002) 2693, doi:10.1088/0954-3899/28/10/313.

[77] G. Cowan, K. Cranmer, E. Gross, and O. Vitells, "Asymptotic formulae for likelihood-based tests of new physics", *Eur. Phys. J. C* **71** (2011) doi:10.1140/epjc/s10052-011-1554-0, 10.1140/epjc/s10052-013-2501-z, arXiv:1007.1727. [Erratum: *Eur. Phys. J. C* **73** (2013) 2501].

[78] ATLAS and CMS Collaborations, LHC Higgs Combination Group, "Procedure for the LHC Higgs boson search combination in Summer 2011", Technical Report ATL-PHYS-PUB-2011-11, CMS NOTE 2011/005, 2011.

[79] CMS Collaboration, "Search for the standard model Higgs boson produced in association with a W or a Z boson and decaying to bottom quarks", *Phys. Rev. D* **89** (2014) 012003, doi:10.1103/PhysRevD.89.012003, arXiv:1310.3687.

[80] K. Hamilton, P. Nason, and G. Zanderighi, "MINLO: Multi-Scale Improved NLO", *JHEP* **10** (2012) 155, doi:10.1007/JHEP10(2012)155, arXiv:1206.3572.

[81] S. Catani, D. de Florian, M. Grazzini, and P. Nason, "Soft-gluon resummation for Higgs boson production at hadron colliders", *JHEP* **07** (2003) 028, doi:10.1088/1126-6708/2003/07/028, arXiv:hep-ph/0306211.

[82] LHC Higgs Cross Section Working Group Collaboration, "Handbook of LHC Higgs Cross Sections: 3. Higgs Properties", arXiv:1307.1347.

[83] R. D. Young and A. W. Thomas, "Octet baryon masses and sigma terms from an SU(3) chiral extrapolation", *Phys. Rev. D* **81** (2010) 014503, doi:10.1103/PhysRevD.81.014503.

[84] MILC Collaboration, "Strange quark condensate in the nucleon in $2+1$ flavor QCD", *Phys. Rev. Lett.* **103** (2009) 122002, doi:10.1103/PhysRevLett.103.122002.

[85] LUX Collaboration, "Improved limits on scattering of weakly interacting massive particles from reanalysis of 2013 LUX data", *Phys. Rev. Lett.* **116** (2016) 161301, doi:10.1103/PhysRevLett.116.161301.

[86] SuperCDMS Collaboration, "New Results from the Search for Low-Mass Weakly Interacting Massive Particles with the CDMS Low Ionization Threshold Experiment", *Phys. Rev. Lett.* **116** (2016) 071301, doi:10.1103/PhysRevLett.116.071301.